



The Distribution and Excitation of CH₃CN in a Solar Nebula Analog

Ryan A. Loomis¹ , L. Ilsedore Cleeves¹ , Karin I. Öberg¹ , Yuri Aikawa² , Jennifer Bergner¹ , Kenji Furuya³ ,
V. V. Guzman⁴ , and Catherine Walsh⁵

¹Harvard-Smithsonian Center for Astrophysics, Cambridge, MA 02138, USA; rloomis@cfa.harvard.edu

²Department of Astronomy, University of Tokyo, 7-3-1 Hongo, Bunkyo-ku, Tokyo 113-0033, Japan

³Center for Computational Sciences, University of Tsukuba, 1-1-1 Tennodai, Tsukuba, Ibaraki 305-8577, Japan

⁴Joint ALMA Observatory, Alonso de Cordova 3107 Vitacura, Santiago de Chile, Chile

⁵School of Physics and Astronomy, University of Leeds, Leeds LS2 9JT, UK

Received 2018 March 2; revised 2018 April 16; accepted 2018 April 27; published 2018 June 1

Abstract

Cometary studies suggest that the organic composition of the early Solar Nebula was rich in complex nitrile species such as CH₃CN. Recent ALMA detections in protoplanetary disks suggest that these species may be common during planet and comet formation, but connecting gas-phase measurements to cometary abundances first requires constraints on formation chemistry and distributions of these species. We present here the detection of seven spatially resolved transitions of CH₃CN in the protoplanetary disk around the T-Tauri star TW Hya. Using a rotational diagram analysis, we find a disk-averaged column density of $N_T = 1.45^{+0.19}_{-0.15} \times 10^{12} \text{ cm}^{-2}$ and a rotational temperature of $T_{\text{rot}} = 32.7^{+3.9}_{-3.4} \text{ K}$. A radially resolved rotational diagram shows the rotational temperature to be constant across the disk, suggesting that the CH₃CN emission originates from a layer at $z/r \sim 0.3$. Through comparison of the observations with predictions from a disk chemistry model, we find that grain-surface reactions likely dominate CH₃CN formation and that in situ disk chemistry is sufficient to explain the observed CH₃CN column density profile without invoking inheritance from the protostellar phase. However, the same model fails to reproduce a solar system cometary abundance of CH₃CN relative to H₂O in the midplane, suggesting that either vigorous vertical mixing or some degree of inheritance from interstellar ices occurred in the Solar Nebula.

Key words: protoplanetary disks

1. Introduction

Observations of comets and meteorites show that the planet and comet forming midplane of the young Solar Nebula had a rich organic volatile composition (e.g., Mumma & Charnley 2011). ALMA observations and the recent *Rosetta* mission have both explicitly shown that comets are abundant in nitrile species such as HCN and CH₃CN (e.g., Cordiner et al. 2014; Le Roy et al. 2015). Tracing the chemistry of this family of organic molecules is of particular interest, as HCN and related nitriles are the starting point for the eventual synthesis of important biomolecules such as glycine (e.g., Bernstein et al. 2002; Powner et al. 2009, 2010; Patel et al. 2015).

In the protoplanetary disks where other planetary systems are just starting to form, the smallest nitriles CN and HCN have long been well known (e.g., Dutrey et al. 1997; van Zadelhoff et al. 2001). Larger nitriles such as HC₃N have only been found more recently (Chapillon et al. 2012), and ALMA is just now beginning to reveal more complex species, such as CH₃CN (Öberg et al. 2015; Bergner et al. 2018). The provenance of these species in disks is unclear, however, and will play a role in setting their final abundances in the forming cometary bodies. Organics may be directly inherited from the chemically rich protostellar stage (e.g., Jørgensen et al. 2016), formed in situ in the disk (e.g., Sakai et al. 2014; Walsh et al. 2014), or both pathways may contribute. If inheritance from the protostellar stage dominates, then nitrile abundances will likely be similar across disks within a given stellar association, while dominant in situ formation may imply that cometary nitrile abundances will be highly disk dependent.

Testing the origin of nitriles such as CH₃CN in disks will require constraining their abundances and formation routes, allowing comparison to predictions from the different inheritance scenarios. As CH₃CN can efficiently form through both gas-phase and grain-surface reactions, however, resolved observations of the disk abundance distribution are necessary to determine its dominant formation route. Thus far, observational constraints have been sparse (Öberg et al. 2015; Bergner et al. 2018). Based on the inferred abundance of CH₃CN in MWC 480, Öberg et al. (2015) concluded that in situ grain-surface chemistry must play an important role. This same chemistry should produce CH₃CN in the disk midplane, affecting the composition of forming comets and planetesimals. Better constraints on the distribution and excitation of CH₃CN in disks are therefore crucial to test this hypothesis and connect disk chemistry with cometary measurements.

In this paper, we present the detection of seven lines of CH₃CN in the disk around TW Hya. A well-studied, old (~ 10 Myr; e.g., Kastner et al. 1997; Weinberger et al. 2013) T-Tauri star, TW Hya hosts the closest (59.5 ± 1 pc; Lindegren et al. 2016) protoplanetary disk, and is a good analog for the Solar Nebula ($0.8 M_{\odot}$, spectral type K7; e.g., Rucinski & Krautter 1983; Bergin et al. 2013). We present the observations and the details of their reduction and imaging in Section 2. In Section 3, we use a rotational diagram analysis to empirically constrain the CH₃CN column density and rotational temperature, both disk-averaged and radially resolved, and compare with predictions from detailed chemical models. In Section 4, we discuss these results and their implications for midplane CH₃CN abundances and incorporation into planetesimals and forming comets. A summary is given in Section 5.

Table 1
Observed CH₃CN Transitions

Transition	Symmetry	Frequency (MHz)	E_u (K)	$S_{ij}\mu^2$ (D ²)	Int. Flux Dens. ^a (mJy km s ⁻¹)	Filter Response (σ)
12 ₀ –11 ₀	A	220747.3 ^b	68.9	183.7 ^c	82 ± 7	17.8
12 ₁ –11 ₁	E	220743.0 ^b	76.0	182.5 ^c	78 ± 7	15.9
12 ₂ –11 ₂	E	220730.3 ^b	97.4	178.6 ^c	41 ± 7	7.2
13 ₀ –12 ₀	A	239137.9 ^b	80.3	199.1 ^c	81 ± 7	13.1
13 ₁ –12 ₁	E	239133.3 ^b	87.5	197.9 ^c	70 ± 7	9.3
13 ₂ –12 ₂	E	239119.5 ^b	108.9	194.3 ^c	28 ± 7	5.7
13 ₃ –12 ₃	A	239096.5 ^b	144.6	188.5 ^c	12 ± 7	3.5

Notes.

^a Velocity-integrated between 2.1 and 3.7 km s⁻¹.

^b Center frequency of collapsed hyperfine components (spacing smaller than channel width).

^c $S_{ij}\mu^2$ of combined hyperfine components.

2. Observations

2.1. Observational Details

TW Hya was observed on 2016 December 29 and 2017 January 09 in Band 6 as part of the ALMA Cycle 4 project 2016.1.01046.S. The first execution block included 43 antennas with projected baseline lengths between 15 and 460 m (11–353 k λ). The second execution block included 47 antennas with projected baseline lengths between 15 and 384 m (11–295 k λ). The on-source integration times were 32 and 31 minutes, respectively, for a total on-source integration time of 63 minutes. The correlator setup was identical for both execution blocks and included a Time Division Mode continuum window centered at 237 GHz with a bandwidth of 2 GHz as well as Frequency Division Mode spectral windows centered at 219.560, 220.740, and 239.112 GHz. These spectral windows had bandwidths of 58.59 MHz and channel spacings of 61 kHz (~ 0.08 km s⁻¹), and they targeted the C¹⁸O $J = 2-1$, CH₃CN $J = 12-11$, and CH₃CN $J = 13-12$ molecular transitions, respectively. As CH₃CN is a prolate symmetric top with C_{3v} symmetry, its rotational spectrum has a k-ladder structure with two spin symmetry states (A/E), allowing a single set of observations to probe a wide range of upper state energies. We cover three transitions in the $J = 12-11$ k-ladder and four transitions in the $J = 13-12$ k-ladder, tabulated in Table 1. The 12₃–11₃ transition was not covered in our spectral setup.

For both executions, the quasar J1058 + 1033 was used for bandpass calibration and the quasar J1037–2934 was used for phase calibration. Callisto was used as the flux calibrator for the first execution, and Ganymede was used as the flux calibrator for the second execution. We additionally used the disk continuum emission in each execution block to perform three rounds of phase self-calibration and one round of amplitude self-calibration in CASA version 4.3. These solutions were then applied to the spectral line observations.

2.2. Results

The observations were first analyzed using a matched filtering technique for identifying weak line emission, described in Loomis et al. (2018c). The C¹⁸O $J = 2-1$ transition was imaged using CLEAN at the native spectral resolution (61 kHz, ~ 0.08 km s⁻¹) with Briggs weighting (robust = 0.5), producing a high signal-to-noise ratio (S/N) image cube (peak S/N = 32). This image cube was then used

as a filter for the CH₃CN spectral windows using the `VISIBLE` code.⁶ From the resultant filter impulse response spectra, we detected all three transitions in the $J = 12-11$ k-ladder covered by the spectral setup and all four transitions in the $J = 13-12$ k-ladder with spectral coverage. The peak filter responses for each transition are given in Table 1.

The seven detected transitions were then individually imaged using CLEAN with natural weighting and a velocity resolution of 0.2 km s⁻¹, centering each image cube on the transition rest frequency. The $J = 13-12$ transitions had a small uv-taper (“outertaper” = 0 $''$ 35) applied to force the synthesized beam to match that of the $J = 12-11$ transitions (1 $''$ 05 \times 0 $''$ 83). The rms of the image cubes was ~ 3.2 mJy beam⁻¹ in each channel, and channel maps are presented in Appendix A. Moment-0 maps of the transitions are shown in Figure 1 and were created by integrating all emission between 2.1 and 3.7 km s⁻¹ with no clipping threshold.

Deprojected and azimuthally averaged radial intensity profiles (Figure 2) were calculated from the moment-0 maps in Figure 1 using an inclination of 7 $^\circ$ and PA of 155 $^\circ$ (Qi et al. 2004; Andrews et al. 2012, 2016). All transitions are centrally peaked, but the beam size is relatively large ($\sim 50-60$ au) compared to the extent of the emission, leaving open the possibility of a ringed morphology at small radii. The transitions all have similar profile shapes, with their relative strengths decreasing with increasing k_a .

Spectra were extracted for each transition using two methods. First, an elliptical mask 3 $''$ 5 in diameter was used (line profiles in Figure 3), which corresponds to a radial extent of ~ 105 au and encapsulates all emission given the radial profiles in Figure 2. Second, a Keplerian mask convolved with the synthesized beam was used to extract the shaded profiles in Figure 3, offering a better estimate of the true flux of each transition. The convolved Keplerian mask was truncated at a radial distance of 105 au, and thus covers the same total solid angle as the elliptical mask. Flux measurements, listed in Table 1, were made by integrating the Keplerian extracted spectra between 2.1 and 3.7 km s⁻¹. Uncertainty on each flux measurement was determined through bootstrapping, repeating the extraction and integration 10,000 times on an identical number of randomly selected nearby emission-free channels (sampled with replacement). The standard deviation of these values is reported as the uncertainty on the flux measurement.

⁶ `VISIBLE` is publicly available at <https://github.com/AstroChem/VISIBLE>.

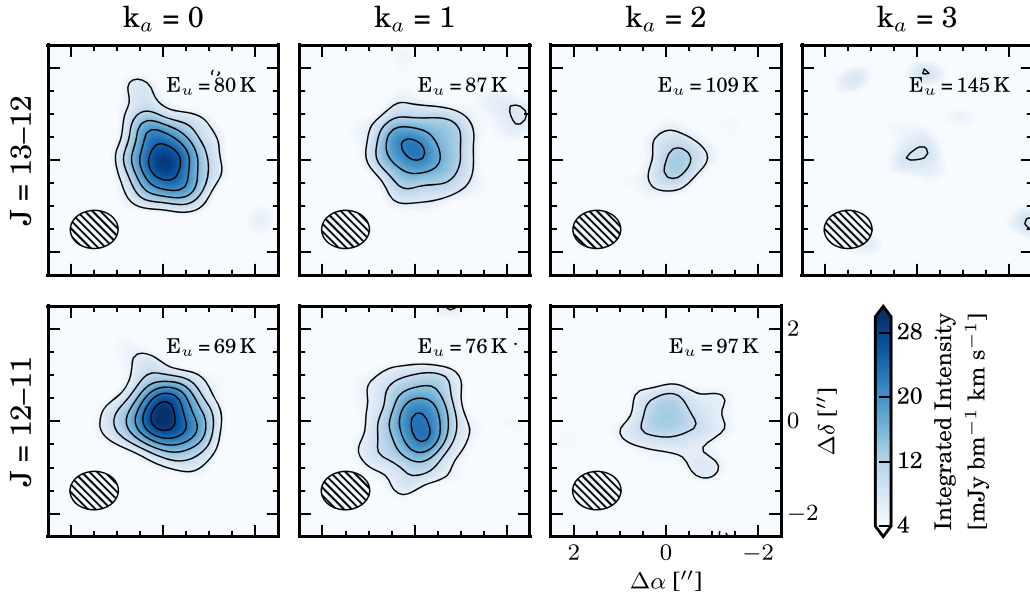


Figure 1. Integrated intensity (moment-0) images of the observed CH₃CN transitions, velocity-integrated between 2.1 and 3.7 km s⁻¹. All panels share the same intensity scale. Contours are [3, 5, 7, ...] × σ, where σ = 2.2 mJy beam⁻¹ km s⁻¹. The synthesized beam is shown in the lower left of each panel.

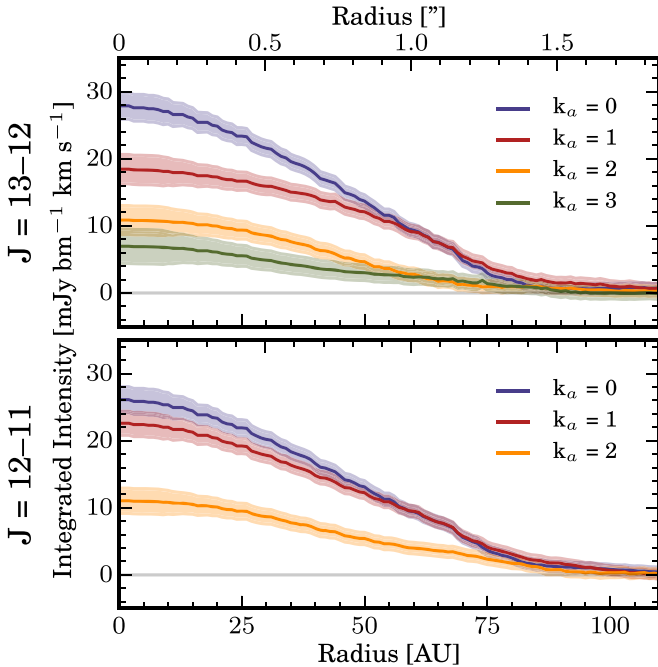


Figure 2. Deprojected and azimuthally averaged radial intensity profiles of the observed CH₃CN transitions. Shaded regions denote 1σ uncertainty levels, where the uncertainty in each radial bin was calculated by dividing the respective moment-0 image rms by the square root of the number of independent measurements in that bin (i.e., the bin circumference divided by the beam size).

3. CH₃CN Column Density and Excitation Temperature

The k-ladder structure of CH₃CN’s rotational spectrum allows multiple transitions to be observed simultaneously, spanning a wide range of upper state energies. With this lever arm, the CH₃CN column density and excitation temperature can be well-constrained through a rotational diagram analysis (e.g., Goldsmith & Langer 1999). We initially assume local thermodynamic equilibrium (LTE) excitation, as the critical densities of the $J = 13-12$ and $J = 12-11$ CH₃CN transitions are $\sim 2.6 \times 10^6$ and $\sim 2.0 \times 10^6$ cm⁻³, respectively, at a

typical disk molecular layer temperature of 40 K (extrapolated to higher J and interpolated in temperature from Shirley 2015). Typical disk gas densities are $> 1 \times 10^6$ cm⁻³, apart from the upper regions of the disk atmosphere ($z/r > 0.6$), which we do not expect these observations to probe.

3.1. Disk-averaged Analysis

We first calculate a disk-averaged column density and excitation temperature. Under an assumption of optically thin emission, the column density of molecules in the upper state of each transition, N_u^{thin} , is related to the emission surface brightness, I_ν , through the equation:

$$I_\nu = \frac{A_{ul} N_u^{\text{thin}} h c}{4\pi \Delta \nu}, \quad (1)$$

where A_{ul} is the Einstein coefficient and $\Delta \nu$ is the linewidth (e.g., Bisschop et al. 2008). The disk-averaged emission intensity is $I_\nu = S_\nu / \Omega$, where S_ν is the flux density and Ω is the solid angle subtended by the source. Substituting for I_ν and inverting Equation (1):

$$N_u^{\text{thin}} = \frac{4\pi S_\nu \Delta \nu}{A_{ul} \Omega h c}. \quad (2)$$

$S_\nu \Delta \nu$ is the integrated flux density reported for each transition in Table 1, and we use the total solid angle covered by the beam-convolved Keplerian mask as an estimate of Ω .

Following Gordy & Cook (1984), the upper state level population N_u can be related to the total column density N_T by the Boltzmann equation:

$$\frac{N_u}{g_u} = \frac{N_T}{Q(T_{\text{rot}})} e^{-E_u/kT_{\text{rot}}}, \quad (3)$$

where g_u is the degeneracy of the upper state level, Q is the molecular partition function, T_{rot} is the rotational temperature, and E_u is the upper state energy. CH₃CN is a symmetric top with C_{3v} symmetry, and the upper state degeneracy g_u can be

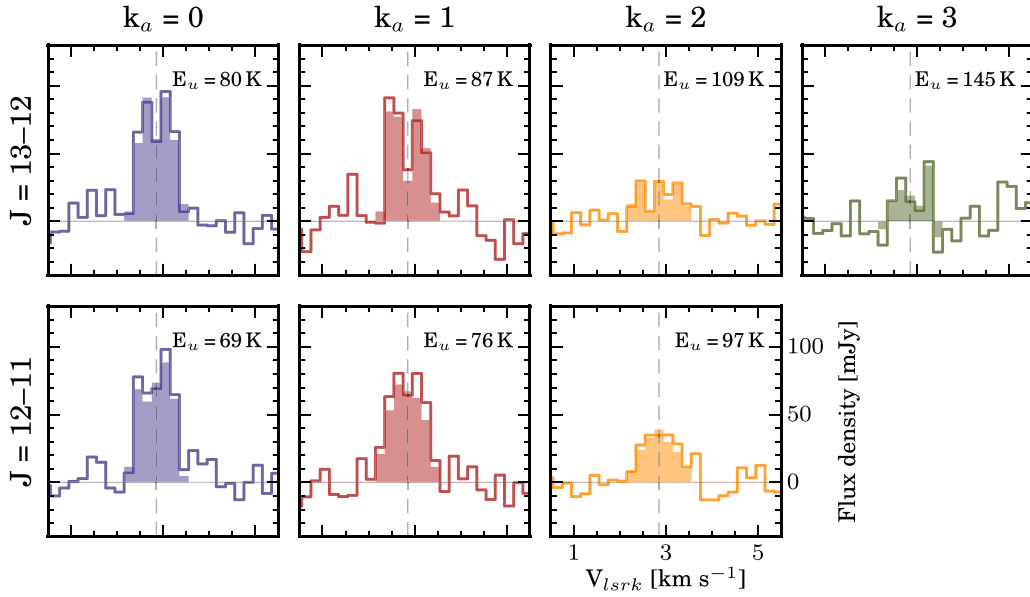


Figure 3. Spectra of the observed CH₃CN transitions. Line profiles were extracted with an elliptical aperture mask 3''5 in diameter, and shaded profiles were extracted using a Keplarian mask convolved with the synthesized beam.

written as

$$g_u = g_J g_K g_I, \quad (4)$$

where $g_J = 2J + 1$, $g_K = 1$ for $K = 0$, and 2 for $K \neq 0$, and g_I is the reduced nuclear spin degeneracy. For CH₃CN, g_I can be defined as

$$g_I = \begin{cases} \frac{1}{3} \left[1 + \frac{2}{(2I+1)^2} \right], & \text{for } K = 0, 3, 6, \dots \\ \frac{1}{3} \left[1 - \frac{2}{(2I+1)^2} \right], & \text{for } K \text{ not divisible by 3.} \end{cases} \quad (5)$$

The partition function Q can be approximated for a molecule with C_{3v} symmetry as

$$Q(T_{\text{rot}}) = \left(\frac{5.34 \times 10^6}{\sigma} \right) \left(\frac{T_{\text{rot}}^3}{B^2 A} \right)^{1/2}, \quad (6)$$

where σ is a unitless symmetry parameter, equal to 3 for a molecule with C_{3v} symmetry, and A and B are the molecular rotational constants. Values for these rotational constants and all other spectral line data were taken from the Spectral Line Atlas of Interstellar Molecules⁷ (F. J. Lovas 2018, private communication, Remijan et al. 2007).

In a conventional rotational diagram analysis (e.g., Goldsmith & Langer 1999), taking the logarithm of Equation (3) allows for a linear least squares regression:

$$\ln \frac{N_u}{g_u} = \ln N_T - \ln Q(T_{\text{rot}}) - \frac{E_u}{kT_{\text{rot}}}. \quad (7)$$

If the level populations, N_u/g_u , are semi-log plotted against the upper state energies, E_u , then the rotational temperature, T_{rot} , and total column density, N_T , can be derived from the best-fit slope and intercept, respectively. Under the assumption of optically thin emission, $N_u^{\text{thin}} = N_u$, Equation (2) can be used to calculate N_u/g_u . The optical depth of the observed CH₃CN transitions is unknown a priori, however. In the case in which the optical depth

$\tau \ll 1$, an optical depth correction factor C_τ must be applied:

$$C_\tau = \frac{\tau}{1 - e^{-\tau}}, \quad (8)$$

and thus the true level populations become

$$N_u = N_u^{\text{thin}} C_\tau, \quad (9)$$

such that Equation (7) is rewritten as

$$\ln \frac{N_u}{g_u} + \ln C_\tau = \ln N_T - \ln Q(T_{\text{rot}}) - \frac{E_u}{kT_{\text{rot}}}. \quad (10)$$

The optical depths of individual transitions are often directly determined through hyperfine ratios or observations of isotopomers, but can also be related back to the upper state level populations:

$$\tau_{ul} = \frac{A_{ul} c^3}{8\pi\nu^3 \Delta\nu} N_u (e^{h\nu/kT_{\text{rot}}} - 1). \quad (11)$$

C_τ can therefore be written as a function of N_u and substituted into Equation (10) to construct a likelihood function $L(N_u, T_{\text{rot}})$ which can then be used for χ^2 minimization.

Given this likelihood function, we use the affine-invariant Markov chain Monte Carlo (MCMC) code `emcee` (Foreman-Mackey et al. 2013) to fit the data and generate posterior probability distributions of both N_u and T_{rot} (see Figure 12 in Appendix B). These probability density functions describe the range of possible column densities and rotational temperatures that are consistent with our observed data. Random draws from these posteriors are plotted in blue in Figure 4, with τ corrected values of N_u/g_u plotted against E_u . We find a disk-averaged column density of $N_T = 1.45_{-0.15}^{+0.19} \times 10^{12} \text{ cm}^{-2}$ and a rotational temperature of $T_{\text{rot}} = 32.7_{-3.4}^{+3.9} \text{ K}$, where parameters and uncertainties are listed as the 50th, 16th, and 84th percentiles from the marginalized posterior distributions, respectively. Corresponding values of τ range between 0.002 and 0.012, confirming that these transitions of CH₃CN are optically thin. These values show a good fit to both the complete data set as well as the individual $J = 12-11$ and $J = 13-12$ k-ladders (shown in orange and red, respectively), consistent with the assumption of LTE excitation.

⁷ Available at <http://www.splatalogue.net>.

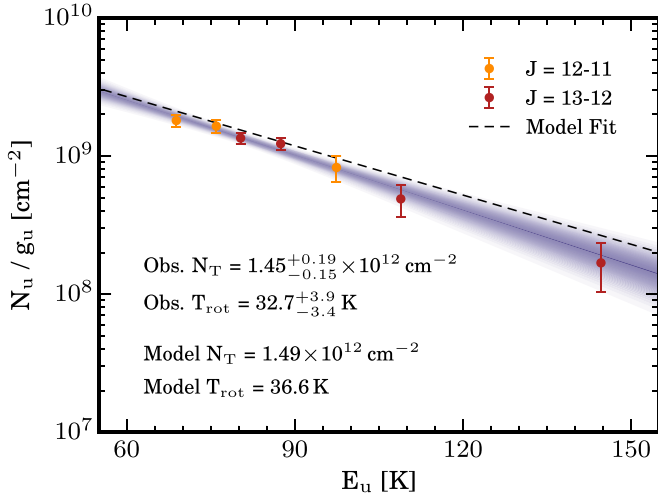


Figure 4. CH₃CN rotational diagram, constructed using disk-averaged intensities. $J = 12-11$ and $J = 13-12$ transitions are shown in orange and red, respectively. Random draws from the fit posteriors are plotted in blue and a fit to simulated observations from the chemical model described in Section 3.3 is plotted by the dashed black line.

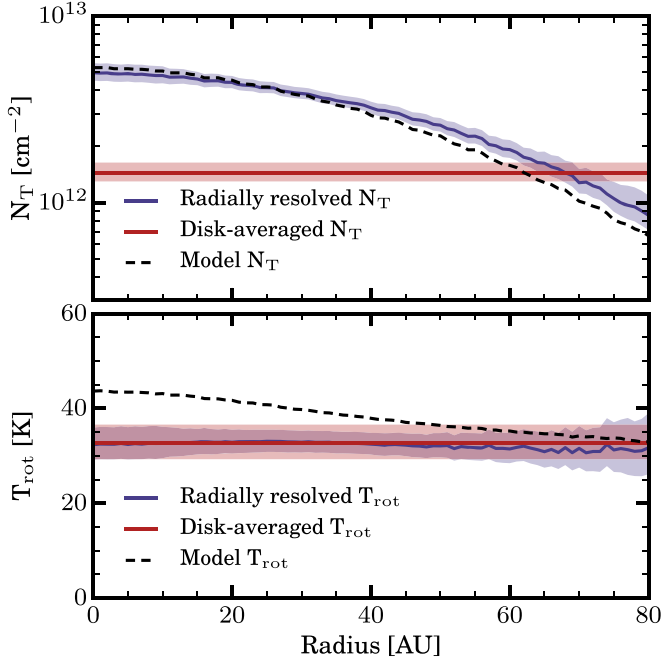


Figure 5. Radial profiles of the fit CH₃CN column density (upper panel) and rotational temperature (lower panel). Best-fit values and 1σ uncertainties are plotted in blue for the radially resolved analysis and in red for the disk-averaged analysis. Fits to the simulated observations described in Section 3.3 are plotted by the dashed black line.

3.2. Radially Resolved Analysis

As the observed CH₃CN transitions are strongly detected and moderately resolved (with a beam size of ~ 50 au), N_T and T_{rot} can be further constrained as a function of radius. We repeat the rotational diagram analysis previously described, but now use intensities from the radial profiles of each transition from Figure 2 rather than disk-averaged intensities. Posterior distributions for N_T and T_{rot} are calculated at intervals of 1 au and are plotted in Figure 5. The rotational diagrams (not shown) remain log-linear and well-behaved out to ~ 70 au but become nonlinear exterior to this distance, leading to the large uncertainties in T_{rot} .

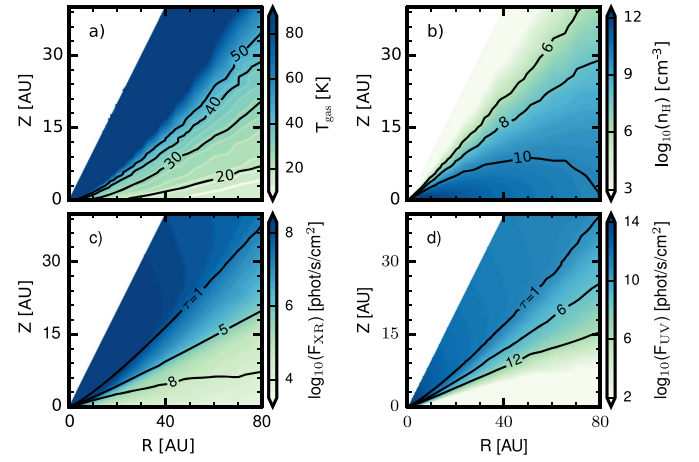


Figure 6. Assumed physical structure of TW Hya used for chemical modeling, taken from Cleeves et al. (2015). Panels (a, b): disk temperature and density structures, respectively. Panels (c, d): X-ray and FUV radiation fields, respectively, with optical depths overlaid as contours.

Table 2
Chemical Model Initial Abundances

Species	Abundance ^a	Species	Abundance ^a
H ₂	5.00×10^{-1}	He	1.40×10^{-1}
N ₂	3.75×10^{-5}	CO	7.00×10^{-6}
H ₂ O(gr)	2.50×10^{-6}	H ₃ ⁺	1.00×10^{-8}
HCO ⁺	9.00×10^{-9}	C ₂ H	8.00×10^{-9}
CS	5.00×10^{-9}	SO	4.00×10^{-9}
C ⁺	1.00×10^{-9}	Si ⁺	1.00×10^{-11}
Mg ⁺	1.00×10^{-11}	Fe ⁺	1.00×10^{-11}

Note.

^a Abundances are relative to the proton density $n_p = 2n_{\text{H}_2}$.

The observed N_T profile decreases with radius from 5 to 0.9×10^{12} cm⁻². This is consistent with the disk-averaged column density of $N_T = 1.45_{-0.15}^{+0.19} \times 10^{12}$ cm⁻², which is overplotted in red in Figure 5. The disk-averaged column density is biased toward the low end of the radially resolved column density range. The majority of the emission (and therefore molecular column) is concentrated in the inner regions of the disk ($R \lesssim 50$ au) and the disk-averaged intensities (integrated out to $R = 105$ au) are therefore diluted. T_{rot} shows a flat radial profile, ranging between 30 and 34 K, consistent with the disk-averaged rotation temperature, $T_{\text{rot}} = 32.7_{-3.4}^{+3.9}$ K.

3.3. Comparison to Chemical Models

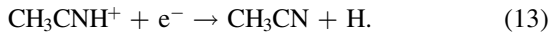
We compare the empirical constraints derived in Sections 3.1 and 3.2 to the predictions of a time-dependent chemical model (Fogel et al. 2011; Cleeves et al. 2014) evolved for 1 Myr. The assumed density and temperature structures, constrained by the TW Hya SED and previous HD observations (Bergin et al. 2013) in Cleeves et al. (2015), are shown in Figure 6 panels (a) and (b), respectively. The initial chemical abundances of the model, listed in Table 2, are based on values from Cleeves et al. (2015) but with updated CO and H₂O depletion factors. CO is depleted by a factor of 20 to approximately compensate for the known carbon depletion in TW Hya (e.g., Favre et al. 2013; Kama et al. 2016; Schwarz et al. 2016). H₂O is depleted in the model by a factor of 100 (e.g., Du et al. 2015). No CH₃CN is included in the initial abundances, and thus all CH₃CN in the model is produced in situ.

The FUV and X-ray radiation fields within the disk (Figure 6, panels c and d) were calculated using the Monte Carlo code and cross sections from Bethell & Bergin (2011), the observed TW Hya FUV spectrum Herczeg et al. (2002, 2004), and a best-fit X-ray model for TW Hya from Cleeves et al. (2015). A reduced cosmic-ray ionization rate was assumed, as TW Hya has been found to have a reduced cosmic-ray ionization rate due to exclusion either by winds or magnetic fields ($\zeta_{\text{CR}} \sim 2 \times 10^{-19} \text{ s}^{-1}$; SSSX model; Cleeves et al. 2015).

The chemical reaction network contains a total of 5970 reactions and 600 species. Within this network, three reactions are primarily responsible for the formation of CH_3CN (Walsh et al. 2014; Wakelam et al. 2015). In the gas phase, formation occurs through the radiative association reaction (Herbst 1985)



followed by dissociative recombination



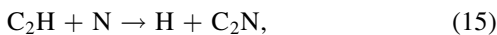
It should be noted, however, that the implicit isomerization of CH_3NCH^+ to CH_3CNH^+ in Equation (12), as written, would likely require a three-body interaction to be efficient (e.g., Anicich et al. 1994) and is not firmly established in the literature as a viable process at the low densities present in protoplanetary disks. An analogous reaction for HNC is also possible



with a disk-integrated HNC/HCN ratio of ~ 0.1 – 0.2 having been previously measured for TW Hya (Graninger et al. 2015). Destruction pathways for gas-phase CH_3CN include UV photodissociation into $\text{CH}_3 + \text{CN}$ and reactions with C^+ .

On grain surfaces, there are two viable formation pathways through a Langmuir–Hinshelwood mechanism: (1) sequential hydrogenation of C_2N or (2) a neutral–neutral grain-surface reaction between CH_3 and CN (Wakelam et al. 2006; Walsh et al. 2014). A reactive desorption efficiency of 1% and a photodesorption yield of 10^{-3} were assumed, with an additional assumption that the CH_3CN molecule always desorbs intact. The validity of these assumptions and their impact are discussed in more detail in Section 4.1.3. Thermal desorption and freeze-out in the model are treated using the Polyani–Wigner relation, with an assumed binding energy of 4680 K for CH_3CN (Collings et al. 2004).

To isolate the respective contributions of gas phase and grain-surface formation mechanisms, we ran the chemical model twice, once with grain-surface reactions turned on and once with them turned off. Figure 7 shows the resultant gas-phase CH_3CN abundance profiles (panels a and b). Both gas-phase and grain-surface reactions contribute to the total CH_3CN reservoir, but form distinct vertical layers. Gas-phase reactions produce CH_3CN in a layer at $z/r \sim 0.5$, where the gas temperature is ~ 50 K. The upper boundary of this layer sits along the FUV $\tau = 1$ surface and is primarily set by the UV photodissociation of CH_3CN . The lower boundary is set where the reactant CH_3^+ is no longer formed in appreciable quantities due to the FUV and X-ray optical depths. Grain-surface reactions meanwhile produce a layer of CH_3CN in the gas phase at $z/r \sim 0.3$ ($T_{\text{gas}} \sim 35$ K), with formation dominated by sequential C_2N hydrogenation. C_2N is primarily formed in the gas phase through the reaction



and then freezes out onto grain surfaces. The upper boundary of the grain-surface CH_3CN layer is set by this freeze-out of C_2N

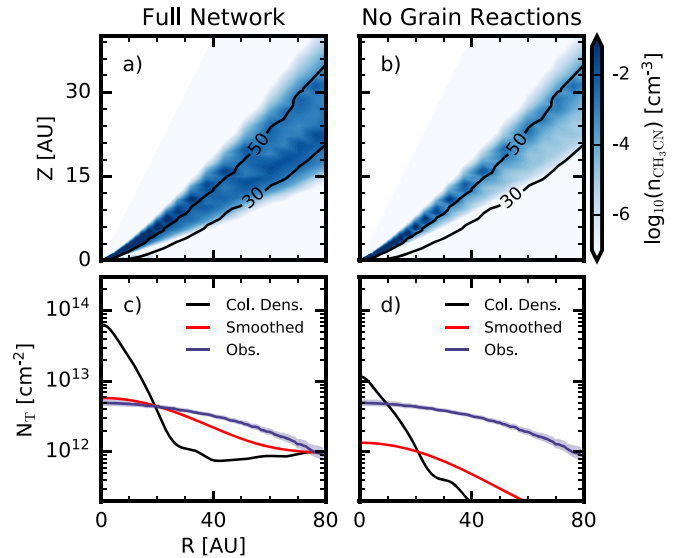


Figure 7. Panels (a, b): CH_3CN gas-phase abundances with grain-surface reactions turned on and off in the model, respectively. Temperature contours of 30 and 50 K are overlaid in black. Panels (c, d): CH_3CN gas-phase column densities for the abundance profiles shown in panels (a) and (b), respectively. Column density profiles smoothed with the synthesized beam are overlotted in red, and the observed column density profile from Figure 5 is overlotted in blue.

and the lower boundary is set by high optical depths limiting photodesorption of CH_3CN off the grain surfaces.

The model abundance profiles were vertically integrated to calculate column density profiles (Figure 7 panels (c) and (d)). The model column density profiles, shown in black, were then convolved with the synthesized beam of the observations to produce the smoothed profiles shown in red. From these profiles, it is clear that grain-surface contributions in the full-network model increase the integrated column density by a factor of 4–10 across the disk. Comparing the beam smoothed model profiles with the observed column density profile in Figure 5, we find that gas-phase reactions alone are insufficient to reproduce the observed column densities, while inclusion of grain-surface reactions reproduces the observed column densities within a factor of 2 across the disk.

Although the beam smoothed profiles allow for a rough comparison to our best-fit observed column density profile, a more detailed comparison requires an identical analysis procedure for both the observations and chemical model results. We therefore used the chemical model output to calculate simulated emission profiles for the observed CH_3CN transitions using the radiative transfer code RADMC-3D (Dullemond et al. 2012). A distance of 59.5 pc, PA of 155° , and stellar mass of $0.8 M_\odot$ (to determine line broadening) were assumed for the radiative transfer (Kastner et al. 1997; Qi et al. 2004; Andrews et al. 2012, 2016). An inclination of 8° was assumed, which approximately accounts for the slight warp in the TW Hya disk (Rosenfeld et al. 2012) and was found to fit our observations relatively well (see Appendix A). Simulated ALMA observations were then calculated for each transition using the `vis_sample` package (Loomis et al. 2018c) and the antenna configuration of the original observations.

From these simulated observations, we repeated the analysis described in Section 3.1 and calculated a disk-averaged rotational temperature and column density, overlotted by a dashed black line in Figure 4. The disk-averaged calculated column density of $N_T = 1.49 \times 10^{12} \text{ cm}^{-2}$ and rotational temperature of $T_{\text{rot}} = 36.6$ K both agree with the observed

column density of $N_T = 1.45^{+0.19}_{-0.15} \times 10^{12} \text{ cm}^{-2}$ and the rotational temperature of $T_{\text{rot}} = 32.7^{+3.9}_{-3.4} \text{ K}$ within the errors.

Similarly, we extracted deprojected and azimuthally averaged radial intensity profiles and repeated the analysis described in Section 3.2 to calculate resolved column density and rotational temperature profiles, overplotted by a dashed black line in Figure 5. Both profiles match the observations relatively well. The model rotational temperature profile is up to $\sim 15 \text{ K}$ warmer than the observations, however, especially at radii $\lesssim 50 \text{ au}$. This might be expected given the distribution of CH_3CN seen in Figure 7, panel (a), peaking at small radii and in a temperature layer $> 50 \text{ K}$. This point is discussed further in Section 4.1.

4. Discussion

4.1. CH_3CN Abundance Structure and Formation Chemistry

4.1.1. Insights from Observations

A rotational diagram analysis of our observations shows that CH_3CN in TW Hya emits at a near constant temperature of $\sim 30\text{--}35 \text{ K}$ across the disk. From our assumed physical model of TW Hya, this temperature suggests emission from a vertical layer at $z/r \sim 0.3$. These first observational constraints on the vertical distribution of CH_3CN are in good qualitative agreement with the layered CH_3CN distribution predicted by the chemical models in Öberg et al. (2015). Similarly, we find that our observed radial column density profile is in good qualitative agreement with the predictions of Walsh et al. (2014) and the observational results of Öberg et al. (2015), which both found column density profiles between $\sim 10^{12}\text{--}10^{13} \text{ cm}^{-2}$ that monotonically decreased with radius.

4.1.2. Comparison of Chemical Models and Observations

We attempted to gain an intuition for the dominant CH_3CN formation pathway by comparing these observational results with two chemical models, with and without grain-surface chemistry. The full chemical network predicts emission that is in remarkably good agreement with our observations, especially given that the model has not been adjusted in any manner to match the data. The model with no grain-surface reactions underpredicts our measured fluxes by over an order of magnitude, suggesting that grain-surface formation of CH_3CN may be the main in situ formation pathway. We additionally find that at all times in the full-network model, the total grain-surface formation rate dominates over the gas-phase formation rate by factors of $\sim 2\text{--}10$. Dominant grain-surface formation is further supported by our observed temperature layer ($\sim 30\text{--}35 \text{ K}$, $z/r \sim 0.3$) being better matched to the grain-surface formation layer than the gas-phase formation layer in Figure 7. The limited spatial resolution of our observations and the caveats of our chemical model presented in Section 4.1.3, however, prevent a more robust quantitative analysis of the relative gas-phase and grain-surface contributions.

Although the full-network model predicts adequate integrated fluxes, some differences remain between the model and observations. First, the radial profile of the model column density is slightly more centrally peaked (even after beam convolution) than the observed column density profile (Figures 5 and 7). Second, although the best-fit disk-averaged column density and rotational temperature are well-matched between the model and observations, the radially resolved model temperature profile is up to 15 K warmer than the observed temperature profile.

These differences are inherently linked; a more centrally peaked column density results in more emission at small radii, where the gas temperature is higher for a given z/r . A number of phenomena therefore could possibly explain these discrepancies. First, a central depletion in the CH_3CN emission cannot be ruled out by our observations, given their relatively low spatial resolution. By stacking the observations and examining the resultant channel maps, we are able to constrain the possible radial extent of such a feature to be less than 16 au (see Appendix A). Second, the chemical model may overestimate gas-phase CH_3CN production, resulting in an enhanced contribution of warm ($\sim 50 \text{ K}$) CH_3CN at small radii. Third, the temperature of the CH_3CN emission is likely sensitive to our assumptions about the physical structure of TW Hya and its FUV and X-ray radiation fields, in particular, as the boundaries of the CH_3CN layer are directly linked to the optical depths of the radiation fields (see Section 3.3). High-resolution observations of smaller molecules, such as HCN, may allow future model refinement by anchoring the assumed initial conditions and disk physical characteristics.

4.1.3. Chemical Model Assumptions and Caveats

A number of assumptions made in our chemical modeling complicate our interpretation of both the observations and models. First, molecules larger than CH_3CN are not included in the model and CH_3CN likely acts as a chemical “sink,” enhancing model abundances. Second, given the uncertainties associated with the dominant gas-phase reaction (see Section 3.3), it is unclear to what extent this pathway contributes to the observed CH_3CN abundance. If the assumed efficiency of this reaction in the model is too high, this may partially explain the higher rotational temperature found for the model compared to the data. Third, we assumed that CH_3CN is always able to photodesorb intact from grain surfaces. Recent investigation on CH_3OH photodesorption suggests that larger molecules such as CH_3CN fragment and thus may have difficulty efficiently photodesorbing intact from grain surfaces (Bertin et al. 2016; Cruz-Diaz et al. 2016; Walsh et al. 2017). If this is the case, reactive desorption may play a larger role as a mechanism for nonthermal CH_3CN desorption. Finally, our model initial conditions assume flat depletion of CO and H_2O across the disk. In reality, spatial variations in depletion and sequestration will result in a modified C/O ratio, which in turn will affect CH_3CN abundances. In particular, the formation of cyanides such as CH_3CN has been shown to be sensitive to carbon and oxygen abundances, with an enhanced C/O ratio resulting in more efficient cyanide formation (Du et al. 2015). The expected nitrile enhancements for older disks with grain growth and radial drift have been tentatively observed by Guzmán et al. (2017), and a similar effect was invoked by Bergin et al. (2016) to explain hydrocarbon rings around TW Hya.

4.2. Implications for Cometary CH_3CN Abundances

Our observations probe gas-phase abundances at a vertical layer in the disk of $z/r \sim 0.3$. In contrast, comets form in the disk midplane and their bulk compositions are primarily set by grain-surface chemical abundances, rather than gas-phase abundances. Interpreting the implications of our observations for the chemical composition of comets, therefore, requires extrapolation to the disk midplane through our chemical model. Figure 8 panels (a) and (b) show the grain-surface abundances of CH_3CN in our chemical models with grain-surface chemistry turned on and off,

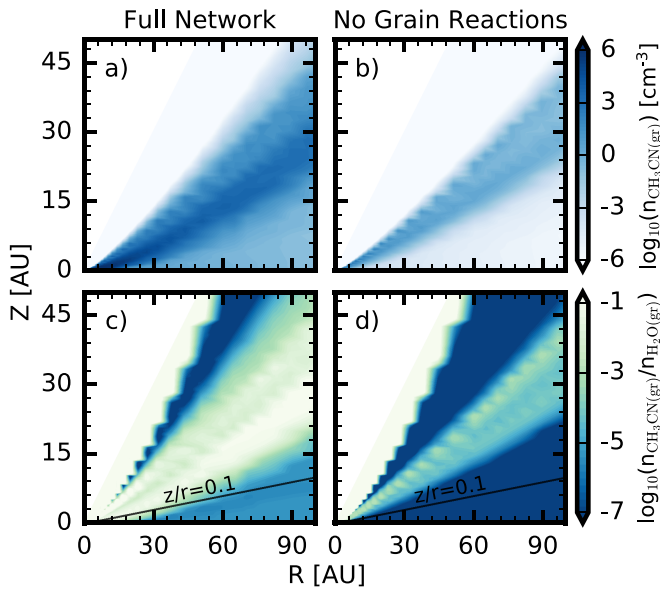


Figure 8. Panels (a, b): CH_3CN abundances in the solid-phase on grain-surfaces, calculated in chemical models with grain-surface reactions turned on and off, respectively. Panels (c, d): $\text{CH}_3\text{CN}(\text{gr})/\text{H}_2\text{O}(\text{gr})$ abundance ratios, calculated from the abundance profiles shown in panels (a) and (b). Note that all CH_3CN in the models is formed in situ, while initial abundances of $\text{H}_2\text{O}(\text{gr})$ are inherited from the protostellar phase.

respectively. Although no CH_3CN is formed on grain-surfaces in the latter model, freeze-out still results in a non-negligible CH_3CN grain-surface abundance.

To compare these grain-surface abundances to measured cometary CH_3CN abundances in the solar system ($\sim 10^{-4}$ relative to H_2O , e.g., Mumma & Charnley 2011), panels (c) and (d) of Figure 8 show $\text{CH}_3\text{CN}(\text{gr})/\text{H}_2\text{O}(\text{gr})$ abundance ratios across the disk model. Initial $\text{H}_2\text{O}(\text{gr})$ abundances in the midplane are inherited from the protostellar phase. We correct for the depletion factor assumed for gas-phase H_2O in the disk surface (e.g., Du et al. 2015; see Section 3.3), as ices in the disk midplane are not expected to be depleted. Gas-phase reactions alone (Figure 8, panel d) are clearly insufficient to reproduce cometary CH_3CN abundances 7×10^{-5} – 3×10^{-4} (e.g., Mumma & Charnley 2011) near the midplane (i.e., $z/r < 0.1$). Incorporation of grain-surface reactions (Figure 8, panel c), however, produces abundances closer to cometary values (up to 5×10^{-4}) in the comet forming regions of the disk ($R \lesssim 10$ – 30 au), consistent with the results of Walsh et al. (2014).

Figure 9 plots $\text{CH}_3\text{CN}(\text{gr})/\text{H}_2\text{O}(\text{gr})$ ratios as a function of z/r at a variety of radii in the disk, comparing these values to the range of known cometary $\text{CH}_3\text{CN}(\text{gr})/\text{H}_2\text{O}(\text{gr})$ ratios. In situ formation in the comet forming zone ($R \lesssim 10$ – 30 au) is insufficient to produce cometary abundances of CH_3CN at the midplane, but can easily yield these abundances at slightly higher disk layers ($z/r > 0.04$), especially at smaller radii. A detailed understanding of the coupling between chemistry and vertical motion of material within the disk will be necessary to determine if CH_3CN produced higher in the disk can be efficiently transported to the midplane for incorporation into comets (e.g., Semenov & Wiebe 2011; Furuya & Aikawa 2014). In particular, such an analysis would require chemical modeling that incorporates both dust settling and turbulent diffusion, as these phenomena have pronounced effects on CH_3CN abundance distributions and the coupling between gas-phase and grain-surface abundances (e.g., Semenov & Wiebe 2011; Öberg et al. 2015).

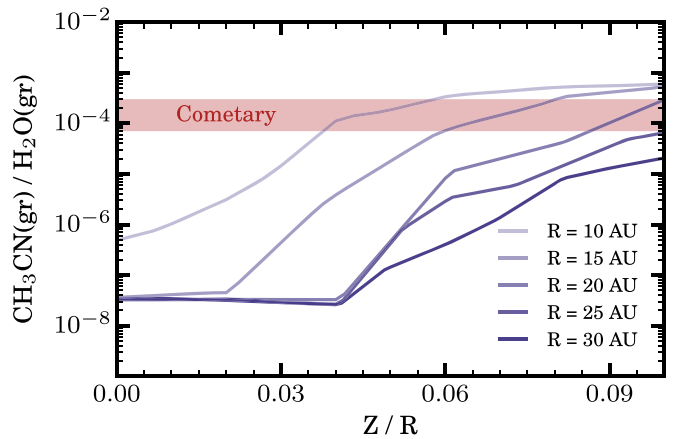


Figure 9. $\text{CH}_3\text{CN}(\text{gr})/\text{H}_2\text{O}(\text{gr})$ abundance ratios from Figure 8, panel (c) (full chemical network) as a function of z/r , taken at different radial slices. The range of values for solar system cometary abundances is shaded in red.

We note that the $\text{CH}_3\text{CN}(\text{gr})/\text{H}_2\text{O}(\text{gr})$ ratios shown in Figure 9 are lower limits, as no inheritance from the protostellar stage is included in our models. Chemical modeling in Eistrup et al. (2016) suggests that such inheritance is possible, with interstellar ice abundances preserved in environments that are shielded from cosmic rays (e.g., TW Hya, Cleaves et al. 2015). Observational evidence for protostellar inheritance of CH_3CN is mixed, however. Öberg et al. (2015) find $\text{CH}_3\text{CN}/\text{HC}_3\text{N}/\text{HCN}$ ratios in MWC 480 that are inconsistent with those found in protostellar regions such as IRAS 16293–2422 (e.g., van Dishoeck et al. 1995), while Bergner et al. (2018) find $\text{CH}_3\text{CN}/\text{HC}_3\text{N}$ ratios in a number of disks that are consistent with protostellar values.

The detection of CH_3CN around TW Hya offers an additional opportunity to evaluate the possibility of protostellar inheritance, as this is the only disk where CH_3OH has been detected thus far (Walsh et al. 2016). We find an approximate $\text{CH}_3\text{CN}/\text{CH}_3\text{OH}$ column density ratio of unity, which is substantially higher than the few percent found in comets and around protostars (Mumma & Charnley 2011; Bergner et al. 2017). As discussed in Bergner et al. (2018), two scenarios could explain this finding: a higher photodesorption efficiency for CH_3CN than CH_3OH (where both species could either be inherited from the protostellar stage or form through in situ grain-surface chemistry), or gas-phase production of nitriles such as CH_3CN could be enhanced by a high C/O ratio as discussed in Section 4.1.3. Thus although our observations are inconsistent with preserved interstellar abundance ratios, it is possible that inheritance contributes to the total CH_3CN abundance in TW Hya.

5. Summary

In summary, we have detected emission from seven transitions of CH_3CN toward TW Hya. A disk-averaged rotational analysis finds a column density of $N_T = 1.82^{+0.25}_{-0.19} \times 10^{12} \text{ cm}^{-2}$ and a rotational temperature of $T_{\text{rot}} = 29.3^{+3.2}_{-2.8} \text{ K}$, and a radially resolved analysis shows this temperature to be flat across the disk. We interpret these results to suggest that CH_3CN emission originates from a layer at $z/r \sim 0.3$ throughout the disk. Comparing these observations with the results of a disk chemistry model, we suggest that grain-surface reactions likely dominate CH_3CN formation. In situ formation in the model is sufficient to explain observed CH_3CN fluxes; though, further model refinement is necessary to accurately reproduce CH_3CN radial and vertical abundance profiles. Finally, we examine the $\text{CH}_3\text{CN}(\text{gr})/\text{H}_2\text{O}(\text{gr})$

ratio predicted by our model and find that cometary abundances of CH_3CN are not present in the disk midplane, but can be found in slightly higher disk layers ($z/r > 0.04$), suggesting that inheritance, dust settling, turbulent mixing, or a combination of these effects is necessary to replicate cometary CH_3CN abundances in the disk midplane.

We thank Edwin Bergin, Jamila Pegues, and Richard Teague for helpful conversations about the data analysis and CH_3CN chemistry. R.A.L. gratefully acknowledges funding from NRAO Student Observing Support. L.I.C. acknowledges the support of NASA through Hubble Fellowship grant HST-HF2-51356.001-A awarded by the Space Telescope Science Institute, which is operated by the Association of Universities for Research in Astronomy, Inc., for NASA, under contract NAS 5-26555. V.V.G. acknowledges support from the National Aeronautics and Space Administration under grant No. 15XRP15_20140 issued through the Exoplanets Research Program. K.I.Ö. acknowledges funding from the Simons Collaboration on the Origins of Life (SCOL). C.W. acknowledges financial support from the University of Leeds. The National Radio Astronomy Observatory is a

facility of the National Science Foundation operated under cooperative agreement by Associated Universities, Inc. This paper makes use of the following ALMA data: ADS/JAO.ALMA #2016.1.01046.S. ALMA is a partnership of ESO (representing its member states), NSF (USA) and NINS (Japan), together with NRC (Canada) and NSC and ASIAA (Taiwan), in cooperation with the Republic of Chile. The Joint ALMA Observatory is operated by ESO, AUI/NRAO, and NAOJ.

Software: Astropy (Astropy Collaboration et al. 2013), CASA (McMullin et al. 2007), casa-python, Matplotlib (Hunter 2007), NumPy (Jones et al. 2001), RADMC-3D (Dullemond et al. 2012), SciPy (van der Walt et al. 2011), vis_sample (Loomis et al. 2018c), VISIBLE (Loomis et al. 2018a, 2018b).

Appendix A Channel Maps

Channel maps of the observed CH_3CN $J = 12-11$ transitions and residuals after subtracting synthesized observations from the full-network chemical model. The observations were imaged with 0.2 km s^{-1} channel spacing and all panels share the same intensity scale. Contours are $[3, 5, 7, \dots] \times \sigma$, where $\sigma = 3.2 \text{ mJy km s}^{-1}$. The synthesized beam is shown in the left panel of each row.

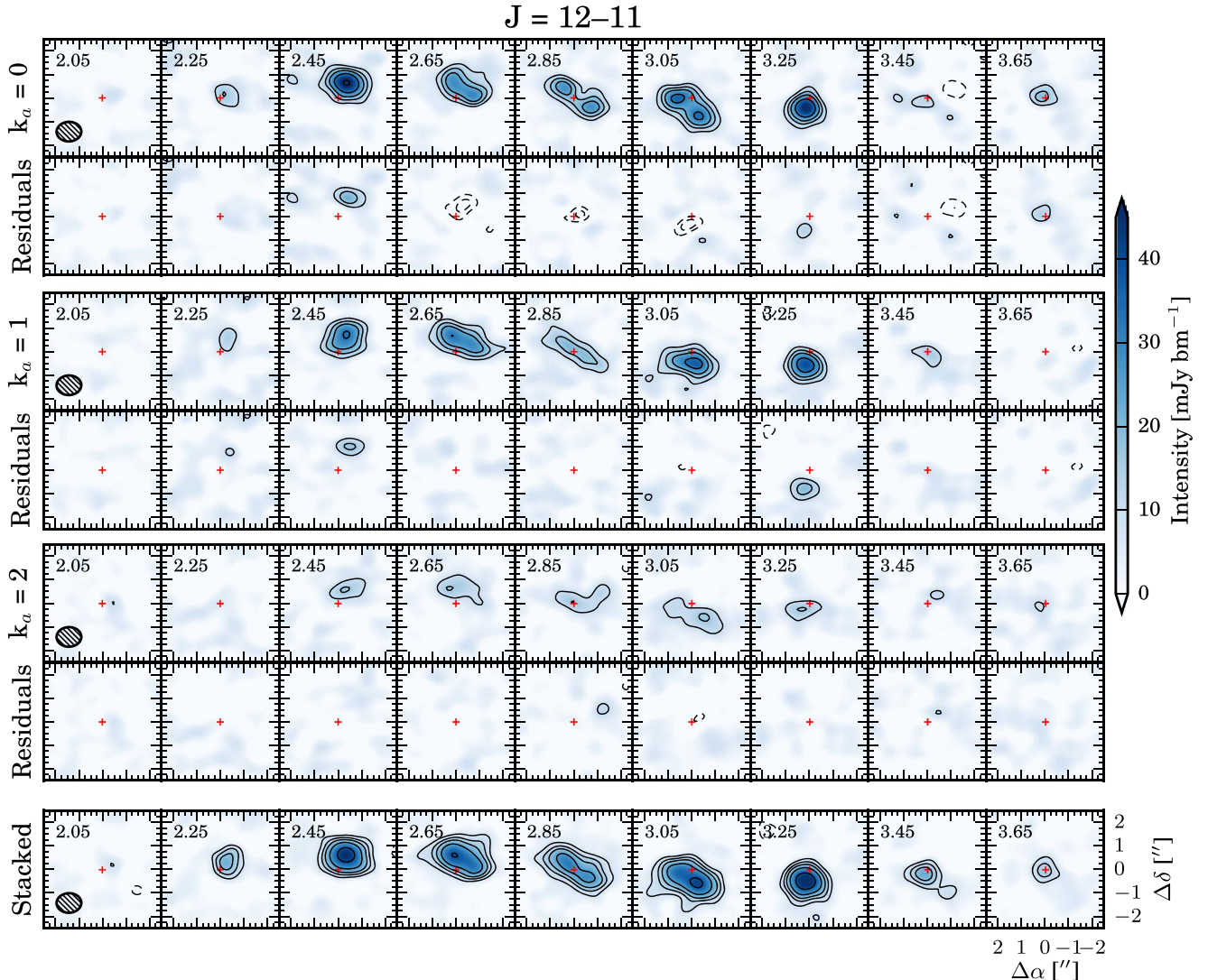


Figure 10. Channel maps of the observed CH_3CN $J = 12-11$ transitions and residuals after subtracting synthesized observations from the full-network chemical model. The observations were imaged with 0.2 km s^{-1} channel spacing and all panels share the same intensity scale. Contours are $[3, 5, 7, \dots] \times \sigma$, where $\sigma = 3.2 \text{ mJy km s}^{-1}$. The synthesized beam is shown in the left panel of each row.

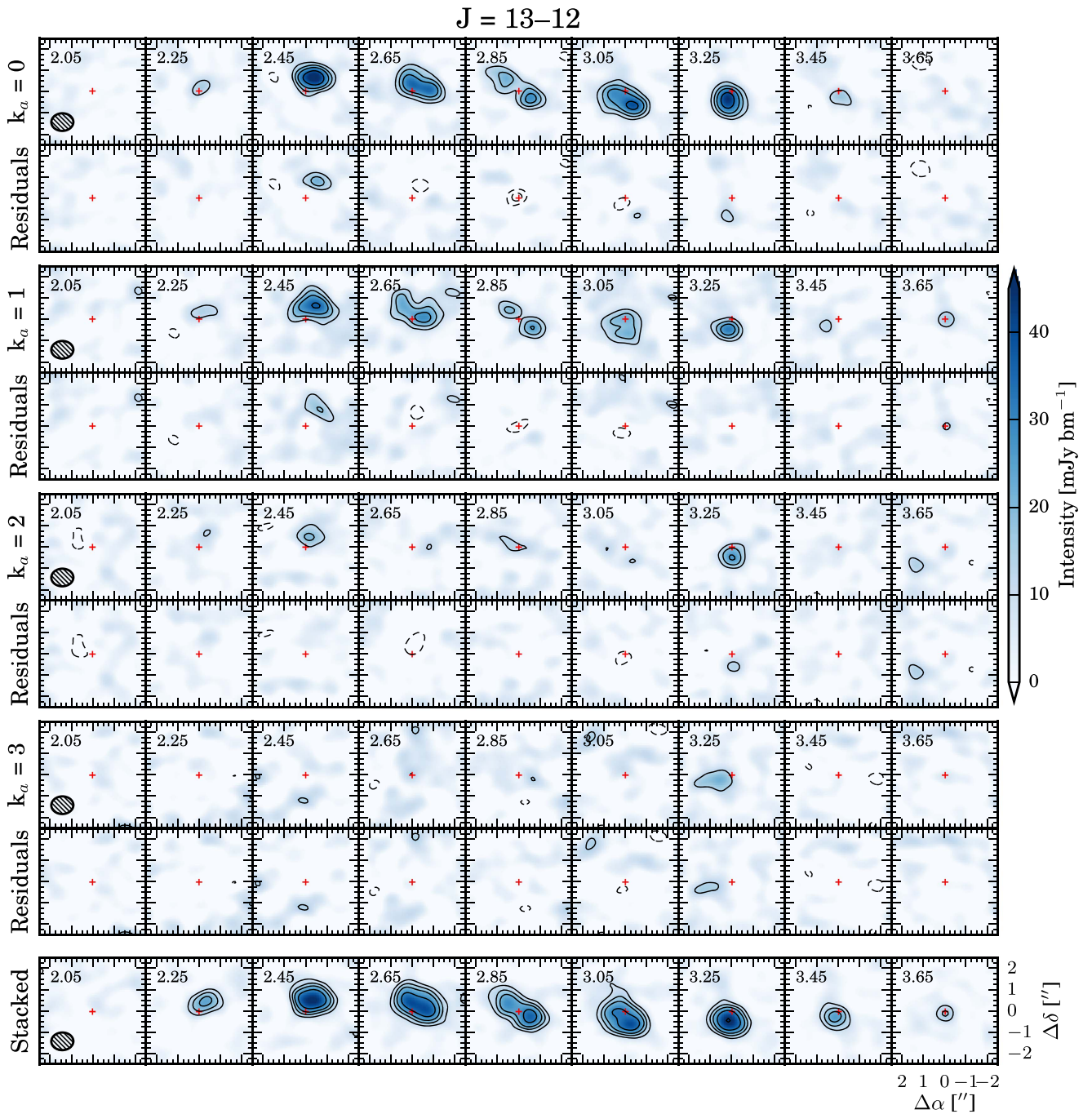


Figure 11. Same as Figure 10, but for the $J = 13-12$ k-ladder of CH_3CN .

model described in Section 3.3 are shown in the figures as well, alternating rows with the observations. Although these residuals are small, a trend is seen where the model over-produces emission in the central channels and under-produces emission at $\pm 0.4 \text{ km s}^{-1}$. This can likely be attributed to the small deviation from Keplerian rotation at small radii in TW Hya (Rosenfeld et al. 2012), which we are only partially able to account for by slightly increasing the overall inclination of our model (from 6° to 8°).

To investigate the distribution of CH_3CN at small radii, we additionally stacked the transitions within each k-ladder to improve the S/N. The filter responses of each transition were used as an estimate of their inherent S/N, and applied as stacking weights when the measurement sets were combined in

the uv-plane. The stacked measurement sets were identically imaged to the individual transitions, and show evidence for emission up to 0.8 km s^{-1} from the systemic velocity. This velocity corresponds to a radius of $\sim 16 \text{ au}$, assuming a stellar mass of $0.8 M_\odot$ and inclination of 7° . The data are therefore compatible with the presence of a depression in CH_3CN surface density at small radii, but constrain the outer radius of such a potential feature to be less than 16 au .

Appendix B MCMC Fit Covariance

A corner plot showing the posterior probability distributions and covariances for the rotational diagram fit shown in Figure 4

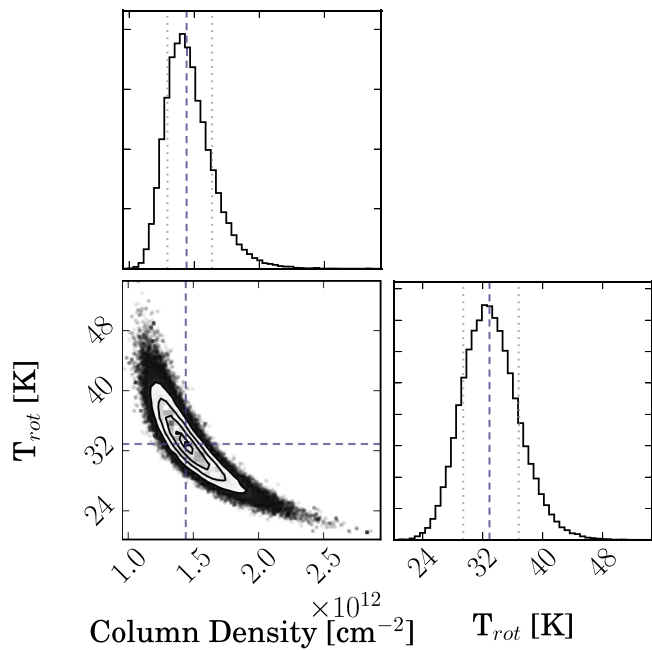









Figure 12. Corner plot showing the posterior probability distributions and covariances for the rotational diagram fit shown in Figure 4. The 16th and 84th percentiles for each parameter are shown by dotted gray lines, with the 50th percentile shown by dashed blue lines.

is shown in Figure 12. Similar covariances are observed for the fit to each radial bin in Figure 5.

ORCID iDs

Ryan A. Loomis  <https://orcid.org/0000-0002-8932-1219>
 L. Ilseore Cleeves  <https://orcid.org/0000-0003-2076-8001>
 Karin I. Öberg  <https://orcid.org/0000-0001-8798-1347>
 Yuri Aikawa  <https://orcid.org/0000-0003-3283-6884>
 Jennifer Bergner  <https://orcid.org/0000-0002-8716-0482>
 Kenji Furuya  <https://orcid.org/0000-0002-2026-8157>
 V. V. Guzman  <https://orcid.org/0000-0003-4784-3040>
 Catherine Walsh  <https://orcid.org/0000-0001-6078-786X>

References

- Andrews, S. M., Wilner, D. J., Hughes, A. M., et al. 2012, *ApJ*, **744**, 162
 Andrews, S. M., Wilner, D. J., Zhu, Z., et al. 2016, *ApJL*, **820**, L40
 Anicich, V. G., Sen, A. D., McEwan, M. J., & Smith, S. C. 1994, *JChPh*, **100**, 5696
 Astropy Collaboration, Robitaille, T. P., Tollerud, E. J., et al. 2013, *A&A*, **558**, A33
 Bergin, E. A., Cleeves, L. I., Gorti, U., et al. 2013, *Natur*, **493**, 644
 Bergin, E. A., Du, F., Cleeves, L. I., et al. 2016, *ApJ*, **831**, 101
 Bergner, J. B., Guzman, V. G., Öberg, K. I., Loomis, R. A., & Piques, J. 2018, *ApJ*, **857**, 69
 Bergner, J. B., Öberg, K. I., Garrod, R. T., & Graninger, D. M. 2017, *ApJ*, **841**, 120
 Bernstein, M. P., Dworkin, J. P., Sandford, S. A., Cooper, G. W., & Allamandola, L. J. 2002, *Natur*, **416**, 401
 Bertin, M., Romanzin, C., Doronin, M., et al. 2016, *ApJL*, **817**, L12
 Bethell, T. J., & Bergin, E. A. 2011, *ApJ*, **740**, 7
 Bisschop, S. E., Jørgensen, J. K., Bourke, T. L., Bottinelli, S., & van Dishoeck, E. F. 2008, *A&A*, **488**, 959
 Chapillon, E., Dutrey, A., Guilloteau, S., et al. 2012, *ApJ*, **756**, 58
 Cleeves, L. I., Bergin, E. A., & Adams, F. C. 2014, *ApJ*, **794**, 123
 Cleeves, L. I., Bergin, E. A., Qi, C., Adams, F. C., & Öberg, K. I. 2015, *ApJ*, **799**, 204
 Collings, M. P., Anderson, M. A., Chen, R., et al. 2004, *MNRAS*, **354**, 1133
 Cordiner, M. A., Remijan, A. J., Boissier, J., et al. 2014, *ApJL*, **792**, L2
 Cruz-Diaz, G. A., Martín-Doménech, R., Muñoz Caro, G. M., & Chen, Y.-J. 2016, *A&A*, **592**, A68
 Du, F., Bergin, E. A., & Hogerheijde, M. R. 2015, *ApJL*, **807**, L32
 Dullemond, C. P., Juhasz, A., Pohl, A., et al. 2012, RADMC-3D: A multi-purpose radiative transfer tool, Astrophysics Source Code Library, ascl:1202.015
 Dutrey, A., Guilloteau, S., & Guelin, M. 1997, *A&A*, **317**, L55
 Eistrup, C., Walsh, C., & van Dishoeck, E. F. 2016, *A&A*, **595**, A83
 Favre, C., Cleeves, L. I., Bergin, E. A., Qi, C., & Blake, G. A. 2013, *ApJL*, **776**, L38
 Fogel, J. K. J., Bethell, T. J., Bergin, E. A., Calvet, N., & Semenov, D. 2011, *ApJ*, **726**, 29
 Foreman-Mackey, D., Hogg, D. W., Lang, D., & Goodman, J. 2013, *PASP*, **125**, 306
 Furuya, K., & Aikawa, Y. 2014, *ApJ*, **790**, 97
 Goldsmith, P. F., & Langer, W. D. 1999, *ApJ*, **517**, 209
 Gordy, W., & Cook, R. L. 1984, *Microwave Molecular Spectra* (3rd ed.; New York: Wiley)
 Graninger, D., Öberg, K. I., Qi, C., & Kastner, J. 2015, *ApJL*, **807**, L15
 Guzmán, V. V., Öberg, K. I., Huang, J., Loomis, R., & Qi, C. 2017, *ApJ*, **836**, 30
 Herbst, E. 1985, *ApJ*, **291**, 226
 Herczeg, G. J., Linsky, J. L., Valenti, J. A., Johns-Krull, C. M., & Wood, B. E. 2002, *ApJ*, **572**, 310
 Herczeg, G. J., Wood, B. E., Linsky, J. L., Valenti, J. A., & Johns-Krull, C. M. 2004, *ApJ*, **607**, 369
 Hunter, J. D. 2007, *CSE*, **9**, 90
 Jones, E., Oliphant, T., Peterson, P., et al. 2001, SciPy: Open Source Scientific tools for Python, <http://www.scipy.org/>
 Jørgensen, J. K., van der Wiel, M. H. D., Coutens, A., et al. 2016, *A&A*, **595**, A117
 Kama, M., Bruderer, S., Carney, M., et al. 2016, *A&A*, **588**, A108
 Kastner, J. H., Zuckerman, B., Weintraub, D. A., & Forveille, T. 1997, *Sci*, **277**, 67
 Le Roy, L., Altwegg, K., Balsiger, H., et al. 2015, *A&A*, **583**, A1
 Lindegren, L., Lammers, U., Bastian, U., et al. 2016, *A&A*, **595**, A4
 Loomis, R., Öberg, K., Andrews, S., et al. 2018a, VISIBLE: VISIBILITY Based Line Extraction, v0.1.0, Zenodo, doi:10.5281/zenodo.1174549
 Loomis, R., Öberg, K., Andrews, S., et al. 2018b, VISIBLE: VISIBILITY Based Line Extraction, Astrophysics Source Code Library, ascl:1802.006
 Loomis, R. A., Öberg, K. I., Andrews, S. M., et al. 2018c, *AJ*, **155**, 182
 McMullin, J. P., Waters, B., Schiebel, D., Young, W., & Golap, K. 2007, in ASP Conf. Ser. 376, *Astronomical Data Analysis Software and Systems XVI*, ed. R. A. Shaw, F. Hill, & D. J. Bell (San Francisco, CA: ASP), 127
 Mumma, M. J., & Chamley, S. B. 2011, *ARA&A*, **49**, 471
 Öberg, K. I., Guzmán, V. V., Furuya, K., et al. 2015, *Natur*, **520**, 198
 Patel, B. H., Percivalle, C., Ritson, D. J., Duffy, C. D., & Sutherland, J. D. 2015, *NatCh*, **7**, 301
 Powner, M. W., Gerland, B., & Sutherland, J. D. 2009, *Natur*, **459**, 239
 Powner, M. W., Sutherland, J. D., & Szostak, J. W. 2010, *JChS*, **132**, 16677
 Qi, C., Ho, P. T. P., Wilner, D. J., et al. 2004, *ApJL*, **616**, L11
 Remijan, A. J., Markwick-Kemper, A., & ALMA Working Group on Spectral Line Frequencies 2007, *BAAS*, **39**, 963
 Rosenfeld, K. A., Qi, C., Andrews, S. M., et al. 2012, *ApJ*, **757**, 129
 Rucinski, S. M., & Krautter, J. 1983, *A&A*, **121**, 217
 Sakai, N., Sakai, T., Hirota, T., et al. 2014, *Natur*, **507**, 78
 Schwarz, K. R., Bergin, E. A., Cleeves, L. I., et al. 2016, *ApJ*, **823**, 91
 Semenov, D., & Wiebe, D. 2011, *ApJS*, **196**, 25
 Shirley, Y. L. 2015, *PASP*, **127**, 299
 van der Walt, S., Colbert, S. C., & Varoquaux, G. 2011, *CSE*, **13**, 22
 van Dishoeck, E. F., Blake, G. A., Jansen, D. J., & Groesbeck, T. D. 1995, *ApJ*, **447**, 760
 van Zadelhoff, G.-J., van Dishoeck, E. F., Thi, W.-F., & Blake, G. A. 2001, *A&A*, **377**, 566
 Wakelam, V., Herbst, E., & Selsis, F. 2006, *A&A*, **451**, 551
 Wakelam, V., Loison, J.-C., Herbst, E., et al. 2015, *ApJS*, **217**, 20
 Walsh, C., Loomis, R. A., Öberg, K. I., et al. 2016, *ApJL*, **823**, L10
 Walsh, C., Millar, T. J., Nomura, H., et al. 2014, *A&A*, **563**, A33
 Walsh, C., Vissapragada, S., & McGee, H. 2017, arXiv:1710.01219
 Weinberger, A. J., Anglada-Escudé, G., & Boss, A. P. 2013, *ApJ*, **762**, 118